

## SOLAR CELLS

# Scalable processing for realizing 21.7%-efficient all-perovskite tandem solar modules

Ke Xiao<sup>1,2</sup>, Yen-Hung Lin<sup>3</sup>, Mei Zhang<sup>1</sup>, Robert D. J. Oliver<sup>3</sup>, Xi Wang<sup>4,5</sup>, Zhou Liu<sup>1</sup>, Xin Luo<sup>1,2</sup>, Jia Li<sup>5</sup>, Donny Lai<sup>5</sup>, Haowen Luo<sup>1</sup>, Renxing Lin<sup>1</sup>, Jun Xu<sup>2</sup>, Yi Hou<sup>4,5</sup>, Henry J. Snaith<sup>3,\*</sup>, Hairen Tan<sup>1\*</sup>

Challenges in fabricating all-perovskite tandem solar cells as modules rather than as single-junction configurations include growing high-quality wide-bandgap perovskites and mitigating irreversible degradation caused by halide and metal interdiffusion at the interconnecting contacts. We demonstrate efficient all-perovskite tandem solar modules using scalable fabrication techniques. By systematically tuning the cesium ratio of a methylammonium-free 1.8-electron volt mixed-halide perovskite, we improve the homogeneity of crystallization for blade-coated films over large areas. An electrically conductive conformal “diffusion barrier” is introduced between interconnecting subcells to improve the power conversion efficiency (PCE) and stability of all-perovskite tandem solar modules. Our tandem modules achieve a certified PCE of 21.7% with an aperture area of 20 square centimeters and retain 75% of their initial efficiency after 500 hours of continuous operation under simulated 1-sun illumination.

**M**onolithic all-perovskite tandem solar cells show great promise for large-scale photovoltaic (PV) applications with the advantage of low-cost solution processing (1–3). However, certified power conversion efficiencies (PCEs), which can reach up to 26.4% (4, 5), have only been achieved in small-area devices with lab-scale spin-coating techniques that limit scalability. To enable large-area fabrication of perovskite films, deposition techniques such as spray coating (6), inkjet printing (7), blade coating (8, 9), slot-die coating (10, 11), and vacuum evaporation (12) have been reported. Solution-based fabrication routes all involve solvent engineering to modulate the crystallization dynamics, but the solvent systems that are in use now for scalable coating of state-of-the-art ~1.5-eV-bandgap perovskite films are incompatible with those of the ~1.8-eV-bandgap wide-bandgap (WBG) perovskites that are needed for all-perovskite tandem solar modules (10). The higher bromide concentration in WBG perovskites leads to variations in crystallization kinetics, and precursor solutions are limited by the low solubility of lead and cesium bromide salts (13). These constraints hinder the scalable fabrication of high-quality WBG perovskites for all-perovskite tandem solar modules (14, 15).

Another challenge in fabricating perovskite solar modules is linked to the reaction of halides and metal electrodes at the interconnecting subcells. The interdiffusion between the perovskite absorber and metal creates deep defect states at either the interface or the bulk of the perovskites (16–19). Unlike small-area perovskite solar cells (PSCs), perovskite solar modules require a three-step laser or mechanical scribing (namely P1, P2, and P3) to connect the subcells in series (20–25). The direct contact between perovskites and metal electrodes at the interconnecting areas between cells leads to subsequent halide-metal interdiffusion and limits the performance and stability of the modules (26). If the tandem-cell recombination junction is a highly conductive transparent conducting oxide (27–29), which is often the case, then metal-to-recombination layer contact will also lead to short-circuiting of one or both of the subjunctions. Injecting two-dimensional (2D) barrier materials, such as 2D nanostructured graphitic carbon nitride, between subcells can inhibit such interdiffusion (26). However, the poor electronic property of these 2D materials adversely causes an undesirable, large hysteresis in the solar modules. Furthermore, adding a 2D diffusion barrier layer between subcells complicates the overall fabrication process and reduces the geometric fill factor (GFF) because it requires two more independent processes (spin-coating and injecting) and necessitates a much wider space gap between subcells. A one-step process to deposit a thin conformal diffusion barrier (CDB) would not only improve cost effectiveness but also reduce the cell-to-module efficiency gap.

In this work, we controlled the homogeneity of crystallization in WBG perovskites over large areas by tuning the content of monovalent inorganic cation cesium. This strategy enabled the fabrication of 1-cm<sup>2</sup> all-perovskite

tandem solar cells with a steady-state PCE of 24.8% through scalable processing techniques. A CDB consisting of atomic-layer-deposited SnO<sub>2</sub> (ALD-SnO<sub>2</sub>) served as both the vertical electron extractor and the lateral diffusion barrier between interconnecting subcells. The CDB inhibited halide-metal interdiffusion and avoided the reaction between perovskites and metal electrode. Using the ALD-SnO<sub>2</sub>-based CDB, we demonstrated all-perovskite tandem solar modules with a certified PCE of 21.7% (aperture area of 20.25 cm<sup>2</sup>). Encapsulated tandem solar modules retained 75% of their initial performance after aging for 500 hours at the maximum power point (MPP) operation under simulated 1-sun illumination in an ambient condition.

We first attempted to blade coat the WBG perovskite films with a composition of Cs<sub>0.2</sub>FA<sub>0.8</sub>PbI<sub>1.8</sub>Br<sub>1.2</sub> (where FA is formamidinium), which was used for the spin-coating process in our previous works (2, 3). The relatively volatile solvent 2-methoxyethanol (2-ME) favors rapid deposition of a uniform perovskite film with low bromide content (21, 30). However, undesirable crystal precipitation occurred when adding WBG perovskite precursors into a 2-ME and dimethyl sulfoxide (DMSO) mixed solvent, given the limited solubility of lead and cesium bromide salts in 2-ME (fig. S1). A stable and transparent precursor solution was obtained when the WBG perovskite precursors were added to the coordinating *N,N*-dimethylformamide (DMF) and DMSO mixed solvent (fig. S1). We used several solvent-quenching methods—such as vacuum flashing, hot casting, and gas quenching—to remove excess DMF and DMSO solvent after the blade-coating step, but none of these methods resulted in dense and uniform perovskite layers (fig. S2). We found that optimizing a range of blading parameter spaces—that is, blade speed, quenching gas pressure, and the gap between the blade and the substrate—was not enough to obtain high-quality, uniform Cs<sub>0.2</sub>FA<sub>0.8</sub>PbI<sub>1.8</sub>Br<sub>1.2</sub> perovskite films (fig. S3). We also attempted to blade-coat films with neat FA cation and a composition of FAPbI<sub>1.8</sub>Br<sub>1.2</sub>; however, the resulting films exhibited an obviously nonperovskite  $\delta$  phase (fig. S4).

We found that the crystal nucleation rate could be controlled by finely tuning the Cs content (denoted as *x* in the Cs<sub>*x*</sub>FA<sub>1-*x*</sub>PbI<sub>1.8</sub>Br<sub>1.2</sub> formula) in conjunction with a gas-assisted blade-coating technique (Fig. 1A). During the gas-quenching step, the nucleation process was initiated under supersaturation conditions, which was evident from the observation that the wet perovskite film turned brown with increased Cs content (fig. S5). We observed the enlargement of grain sizes and the flattening of the film surface with higher Cs incorporation (up to 35 mol %) into the perovskite. For film where *x* is equal to 0.35 (Cs<sub>0.35</sub>FA<sub>0.65</sub>PbI<sub>1.8</sub>Br<sub>1.2</sub>),

<sup>1</sup>National Laboratory of Solid State Microstructures, Jiangsu Key Laboratory of Artificial Functional Materials, College of Engineering and Applied Sciences, Frontiers Science Center for Critical Earth Material Cycling, Nanjing University, Nanjing 210023, China. <sup>2</sup>School of Electronics Science and Engineering, Nanjing University, Nanjing 210093, China. <sup>3</sup>Clarendon Laboratory, Department of Physics, University of Oxford, Oxford OX1 3PU, UK. <sup>4</sup>Department of Chemical and Biomolecular Engineering, National University of Singapore, 4 Engineering Drive 4, Singapore 117585, Singapore. <sup>5</sup>Solar Energy Research Institute of Singapore (SERIS), National University of Singapore, 7 Engineering Drive 1, Singapore 117574, Singapore.

\*Corresponding author. Email: harentan@nju.edu.cn (H.T.); henry.snaith@physics.ox.ac.uk (H.J.S.)

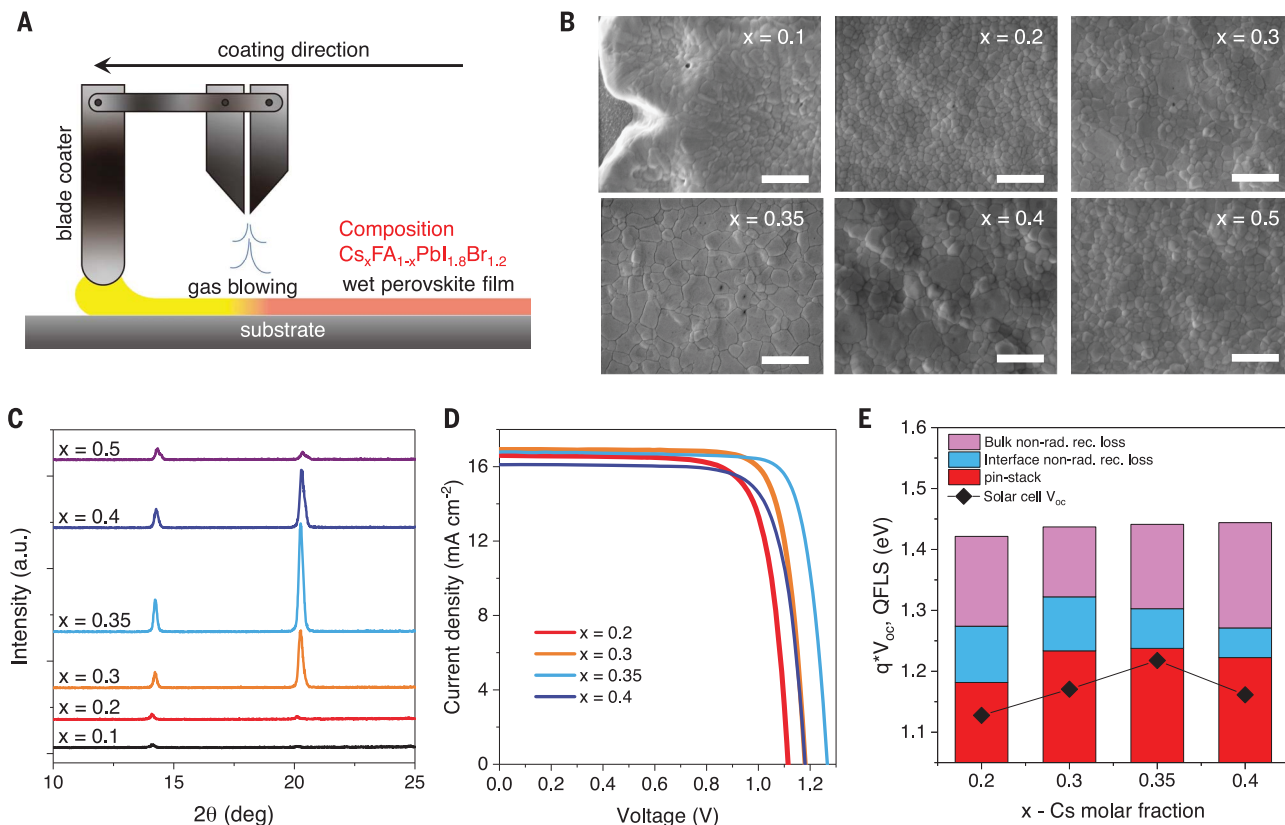


**Fig. 1. Fabrication of  $\text{Cs}_x\text{FA}_{1-x}\text{PbI}_{1.8}\text{Br}_{1.2}$  WBG perovskite films using blade coating.** (A) Schematic illustration of gas-assisted blade coating. (B and C) SEM images (B) and x-ray diffraction patterns (C) of  $\text{Cs}_x\text{FA}_{1-x}\text{PbI}_{1.8}\text{Br}_{1.2}$  perovskite films. The scale bars in the SEM images are  $1 \mu\text{m}$ . a.u., arbitrary units. (D)  $J$ - $V$  curves of champion

$\text{Cs}_x\text{FA}_{1-x}\text{PbI}_{1.8}\text{Br}_{1.2}$  PSCs. (E) QFLS calculated from the PLQY for the respective perovskite films and the perovskites with transport layer stacks that were investigated in the study. The Shockley-Queisser radiative limit and the experimental  $V_{oc}$  are plotted for each composition. non-rad. rec. loss, nonradiative recombination loss.

we observed the largest grain sizes with a uniform surface, as observed from scanning electron microscopy (SEM) and atomic force microscopy (AFM) images (Fig. 1B and fig. S6). It should be noted that the grains or grain boundaries seen in SEM and AFM observations are only features of morphological domains or domain boundaries (31). The  $\text{Cs}_{0.35}\text{FA}_{0.65}\text{PbI}_{1.8}\text{Br}_{1.2}$  perovskite film also exhibited the highest crystallinity, as indicated by the x-ray diffraction patterns (Fig. 1C and fig. S7A).

The grazing-incidence wide-angle x-ray scattering and the corresponding diffraction mottling intensity profiles integrated along the ring with scattering vector ( $q$ ) equal to  $1.0 \text{ \AA}^{-1}$  are shown in fig. S8. For blade-coated  $\text{Cs}_{0.35}\text{FA}_{0.65}\text{PbI}_{1.8}\text{Br}_{1.2}$  perovskite films, the diffraction mottling at the azimuth angles of  $45^\circ$  ( $135^\circ$ ) and  $90^\circ$  became distinct compared with the ambiguous diffraction mottling at  $60^\circ$  ( $120^\circ$ ) for spin-coated  $\text{Cs}_{0.2}\text{FA}_{0.8}\text{PbI}_{1.8}\text{Br}_{1.2}$  perovskite films. This new pattern implied that a distinct stacking orientation developed along with (100) crystallographic planes for the WBG perovskite films deposited through gas-assisted blade coating. Large crystal grains grown perpendicular to the substrate throughout the whole film were observed in blade-coated

perovskite films (fig. S8). By contrast, smaller grains with multiple grain boundaries throughout the film were formed for spin-coated films. We observed that the grain orientation and crystallinity of blade-coated films were strongly related to the Cs content, which had only a weak impact on spin-coated films (fig. S9).

We noted a linear increase in the bandgap of  $\text{Cs}_x\text{FA}_{1-x}\text{PbI}_{1.8}\text{Br}_{1.2}$  perovskites when  $x$  was increased up to 0.35. However, nonlinearity in the optical bandgap was seen when  $x$  was greater than 0.35 (fig. S10), which may have been caused by phase segregation in the perovskite films (fig. S7B). Perovskites with  $x$  less than 0.3 suffered from light-induced phase segregation under high illumination intensities (i.e., 10 suns), which was evident from the multiple emission peaks observed in the steady-state photoluminescence (PL) spectra (fig. S11). The reduced photoinduced phase segregation in film with  $x$  equal to 0.35 could be due to the reduced lattice strain with a higher Cs ratio (32) and/or the change in thermodynamics related to the intermixing of ions or ion migration within the crystal lattice (33, 34).

We then evaluated the effect of Cs content on the optoelectronic properties and PV performance of inverted positive-intrinsic-

negative (p-i-n)-structured WBG PSCs. The  $\text{Cs}_{0.35}\text{FA}_{0.65}\text{PbI}_{1.8}\text{Br}_{1.2}$  perovskite films showed the longest carrier lifetime, as determined by PL decay (fig. S12). The performance distribution, external quantum efficiency (EQE), and steady-state power output of various  $\text{Cs}_x\text{FA}_{1-x}\text{PbI}_{1.8}\text{Br}_{1.2}$ -based devices are summarized in fig. S13, suggesting an optimal composition of  $\text{Cs}_{0.35}\text{FA}_{0.65}\text{PbI}_{1.8}\text{Br}_{1.2}$ . The champion  $\text{Cs}_{0.35}\text{FA}_{0.65}\text{PbI}_{1.8}\text{Br}_{1.2}$  device achieved a PCE of 17.2%, with an open-circuit voltage ( $V_{oc}$ ) of 1.266 V, a short-circuit current density ( $J_{sc}$ ) of  $16.8 \text{ mA cm}^{-2}$ , and a fill factor (FF) of 80.9% (Fig. 1D and table S1). The blade-coated devices ( $x = 0.35$ ) exhibited comparable performance to the spin-coated ones ( $x = 0.20$ ; fig. S14), and the spin-coated devices with various Cs contents showed similar performance (fig. S15).

To understand how the Cs content ( $x = 0.2$  to 0.4) affects the performance of blade-coated cells, we measured the transient photovoltage decay under open-circuit conditions (fig. S16). The photovoltage-decay lifetime  $\tau$  of the  $\text{Cs}_{0.35}\text{FA}_{0.65}\text{PbI}_{1.8}\text{Br}_{1.2}$  device ( $86 \mu\text{s}$ ) was higher than that of the  $\text{Cs}_{0.2}\text{FA}_{0.8}\text{PbI}_{1.8}\text{Br}_{1.2}$  device ( $31 \mu\text{s}$ ), indicating a reduced recombination when the ratio of Cs was increased from 0.2 to

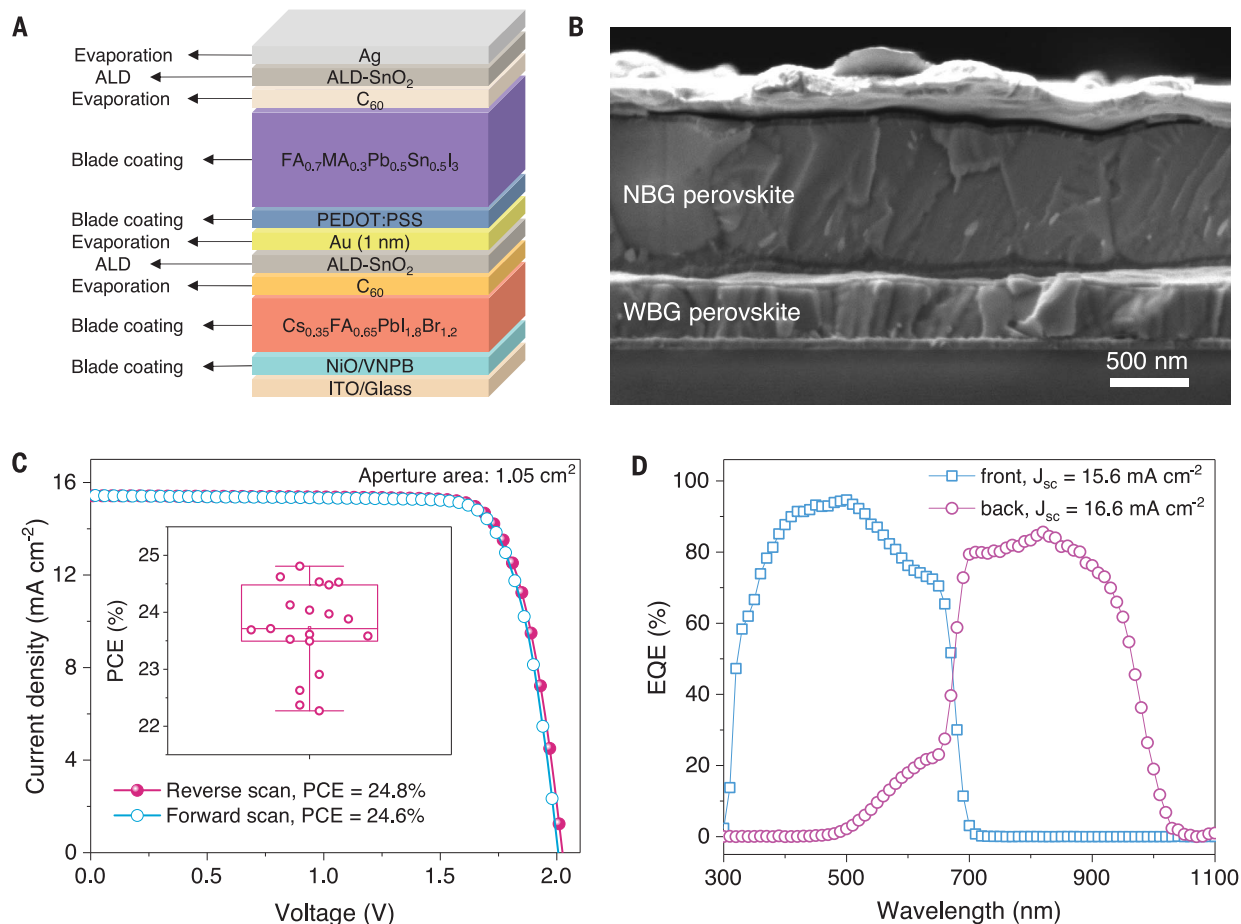


**Fig. 2. Full fabrication of all-perovskite tandem solar cells using scalable techniques.** (A) Configuration schematic of an all-perovskite tandem device fully fabricated using scalable techniques. The processing technique for each layer is indicated to the left. (B) Cross-sectional SEM image of the all-perovskite tandem device. (C)  $J$ - $V$  curves of the champion tandem solar cell (aperture

area of  $1.05 \text{ cm}^2$ ) deposited on a 2.5-cm-by-2.5-cm substrate. The inset shows the PCE distribution of 19 devices, where the boxes and whiskers represent the standard deviation and the maximum and minimum of the distributions, respectively. (D) EQE curves of the champion device. The front and back subcells have integrated  $J_{sc}$  values of  $15.6$  and  $16.6 \text{ mA cm}^{-2}$ , respectively.

0.35. To further elucidate  $V_{oc}$  improvement of the PSCs with various Cs ratios, we investigated the PL quantum yield (PLQY) of isolated perovskite thin films and device stacks that had both charge-transporting layers present (fig. S17). These measured PLQY values were then used to derive the quasi-Fermi level splitting (QFLS) in the respective perovskite materials and p-i-n stacks (Fig. 1E). Notably, the calculated QFLS values of the p-i-n stacks corroborated well with the  $V_{oc}$  of the WBG PSCs and suggested that nonradiative recombination losses were reduced by increasing Cs to an  $x$  of 0.3 to 0.35.

We then investigated the uniformity of  $\text{Cs}_{0.35}\text{FA}_{0.65}\text{PbI}_{1.8}\text{Br}_{1.2}$  perovskite films that were blade coated over a large area (6-cm-by-6-cm substrate; fig. S18). We patterned eight solar cells over a single substrate with each device pixel having an aperture area of  $2.2 \text{ cm}$  by  $1.125 \text{ cm}$  ( $2.475 \text{ cm}^2$ ), as illustrated in the inset of fig. S19A. All eight devices showed nearly identical device performance with a minor PCE standard deviation of 0.03% (fig.

S19 and table S2). The narrowly distributed device performance indicates the effectiveness of the blade-coating method to achieve large-area uniformity for WBG perovskite films. By contrast, the devices distributed on the 6-cm-by-6-cm substrate by spin coating exhibited larger variations in performance among eight pixels (PCE standard deviations of 0.36 and 0.63% for  $\text{Cs}_{0.35}\text{FA}_{0.65}\text{PbI}_{1.8}\text{Br}_{1.2}$  and  $\text{Cs}_{0.2}\text{FA}_{0.8}\text{PbI}_{1.8}\text{Br}_{1.2}$ , respectively). It should be noted that tuning the Cs content is likely not the only way to achieve high-quality, uniform WBG perovskite films, so further work in optimizing the blading parameter space, precursor solvent, and additives may also lead to similar or even better-quality films.

To realize tandem solar cells with scalable manufacturing techniques, we used blade coating to replace spin coating in all of the solution-based processes, including the fabrication of narrow bandgap (NBG) perovskite film ( $\text{MA}_{0.3}\text{FA}_{0.7}\text{Pb}_{0.5}\text{Sn}_{0.5}\text{I}_3$ , where MA is methylammonium) and hole transport layers (Fig.

2A). All other material layers were deposited through either thermal evaporation or ALD, which are both scalable processes already used in PV manufacturing. The blade-coated NBG PSCs ( $0.049 \text{ cm}^2$ ) delivered a champion PCE of 19.0% (steady-state PCE of 19.0%) and good reproducibility (fig. S20). Monolithic all-perovskite tandem solar cells, consisting of a  $\sim 400$ -nm-thick WBG perovskite and a  $\sim 950$ -nm-thick NBG perovskite (Fig. 2B), were fabricated entirely with scalable techniques. The current density-voltage ( $J$ - $V$ ) and EQE curves of the best-performing tandem device with an aperture area of  $1.05 \text{ cm}^2$  are presented in Fig. 2, C and D, respectively. An average PCE of  $23.7 \pm 0.7\%$  was obtained from 19 devices (inset of Fig. 2C). The champion device had a PCE of 24.8% from the reverse scan, with a  $V_{oc}$  of 2.025 V, a  $J_{sc}$  of  $15.4 \text{ mA cm}^{-2}$ , and a FF of 79.4%. A highest efficiency of 25.1% (average PCE of  $24.2 \pm 0.6\%$  from 44 devices) was obtained for  $0.049\text{-cm}^2$  tandem devices (fig. S21). The relatively modest PCE difference between

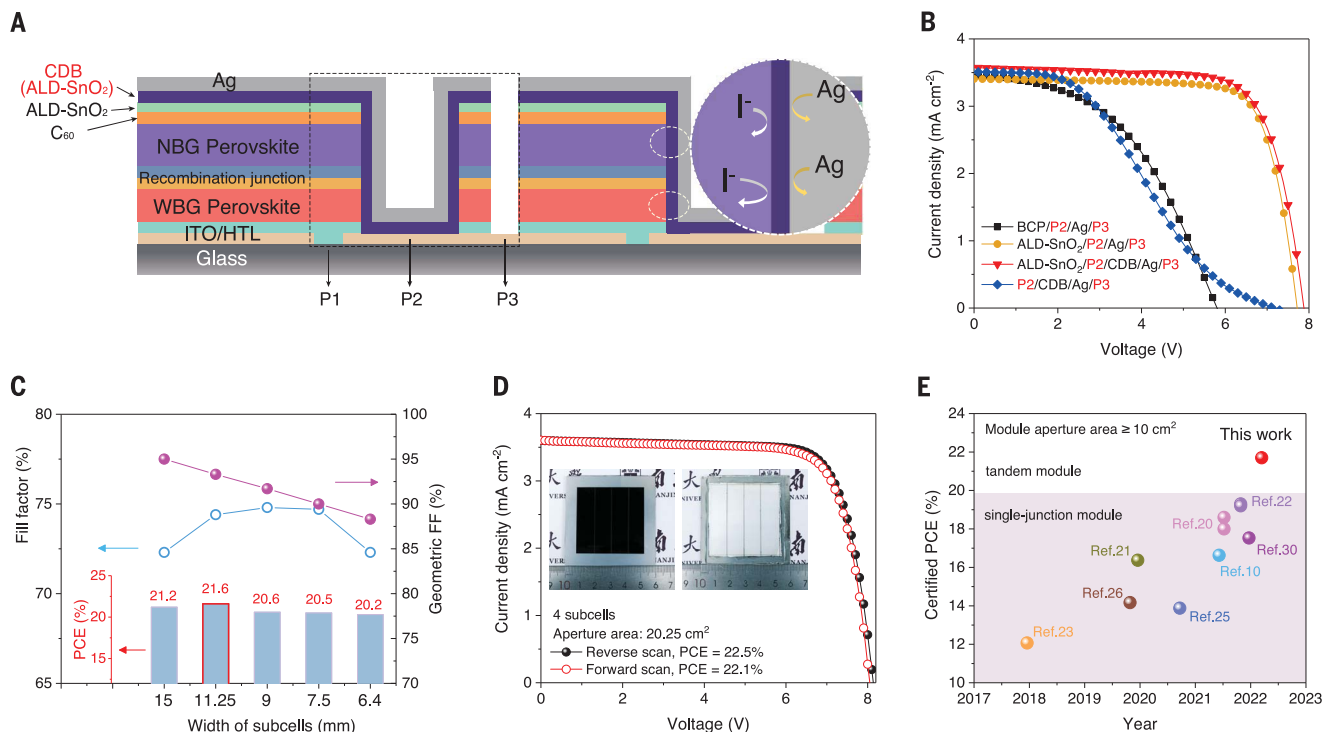


**Fig. 3. All-perovskite tandem modules.** (A) Schematic diagram of the structure of the series-connected all-perovskite tandem module with CDB to prevent ion diffusion. HTL, hole transport layer. (B) *J*-*V* curves of different module configurations. BCP, bathocuproine. (C) Relationship between the FF, GFF, and efficiency of modules. The arrows indicate GFF (purple), FF (blue),

and PCE (red). (D) *J*-*V* curves of the champion all-perovskite tandem module (aperture area of 20.25 cm<sup>2</sup>, four subcells in series). The inset shows photos of the front side (left) and back side (right) of the module. (E) Summary of publicly reported, independently certified PCEs of perovskite solar modules (aperture area ≥10 cm<sup>2</sup>).

the 1.05- and 0.049-cm<sup>2</sup> cells suggests good scalability for all-perovskite tandem solar cells.

We fabricated all-perovskite tandem solar modules on 6-cm-by-6-cm substrates. The long-term stability and efficiency degradation of perovskite tandem modules is attributed in part to the interfacial halide-metal electrode reaction at the P2-scribed regions between the interconnecting subcells (Fig. 3A). To address this challenge, we devised an electrically conductive CDB by depositing ~10-nm-thick ALD-SnO<sub>2</sub> after P2 scribing to avoid interdiffusion and reaction between the perovskite and metal electrode (figs. S22 and S23). The CDB layer not only reduces the module manufacturing complexity but also enables a much narrower P2-scribed region (thus higher GFF and module efficiency) compared with injecting a wide insulating 2D barrier material at the interconnecting regions (26). We noted that another ALD-SnO<sub>2</sub> protective layer (~10 nm) deposited on C<sub>60</sub> before the P2 process to be performed under ambient conditions (Fig. 3B). We speculate that this compact protective layer prevented NBG perovskite from oxidation during exposure to ambient air (2).

In comparison, all of the modules that did not have the ALD-SnO<sub>2</sub> protective layer before

performing the P2 process showed inferior performance. After the P2 process, the ALD-SnO<sub>2</sub>-based CDB layer prevented direct contact between the metal electrode and the perovskite absorber at the P2-scribed regions. It also prevented direct contact between the metal electrode and the conductive poly(3,4-ethylenedioxythiophene) polystyrene sulfonate (PEDOT:PSS) in the recombination layer, which could otherwise lower the shunt resistance. The current-voltage measurements, performed at the ITO/ALD-SnO<sub>2</sub>/Ag junction (where ITO is indium tin oxide), showed good ohmic contact with low vertical resistance (fig. S24), suggesting that this semiconducting CDB layer allowed effective electrical interconnection between subcells. The CDB layer improved both the efficiency and reproducibility of the all-perovskite tandem solar modules (fig. S25A).

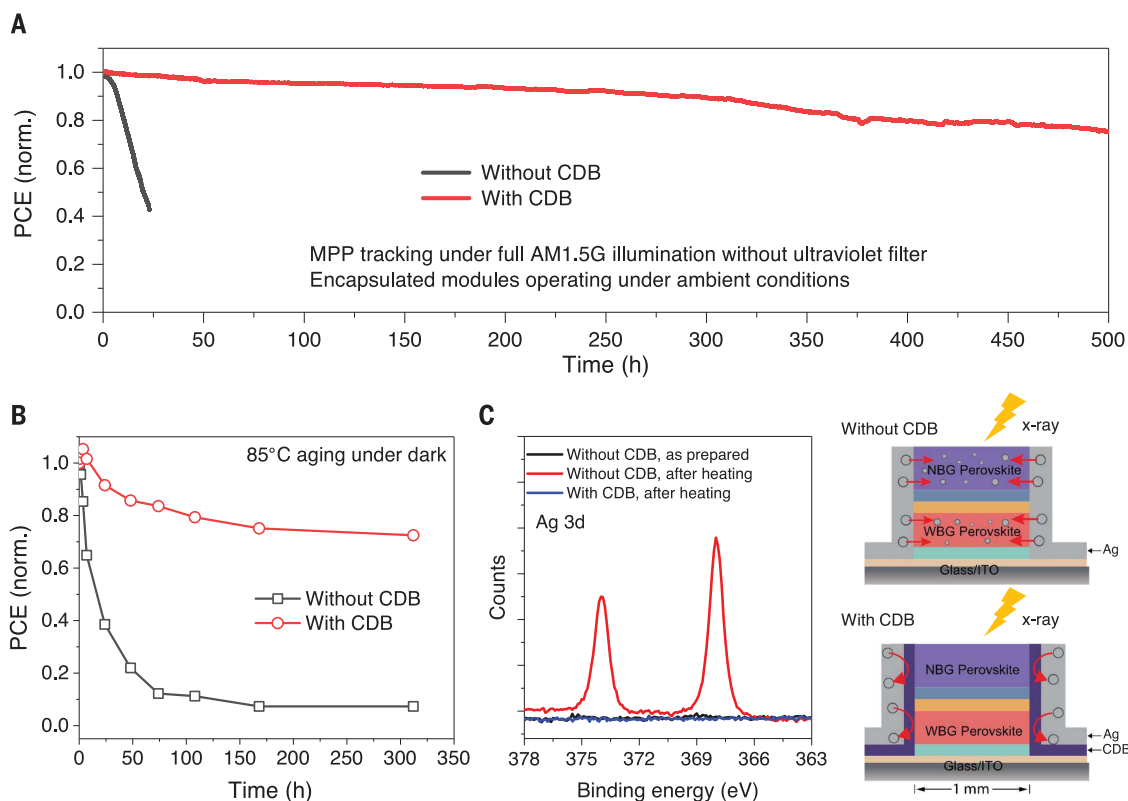
We investigated how the subcell width would affect the performance of tandem modules. Increasing the subcell width allows for a higher GFF and thus potentially higher module efficiency, but this strategy adversely introduces a higher series resistance and hence reduces the FF. We fabricated modules that had three to seven subcells with a fixed total area, corresponding to subcell widths ranging from 15 to 6.4 mm (fig. S25B). The GFF is calculated

to decrease linearly from 95.0 to 88.3% as the number of subcells increases (Fig. 3C and fig. S26). The optimal performance was achieved for the four-subcell tandem modules with a width of 11.25 mm and a GFF of 93.3% (Fig. 3C and table S3). We expect that laser scribing (35, 36), instead of mechanical scribing, for P2 and P3 processings could allow for an even higher GFF and thus higher module efficiency, given that the subcell widths of tandems that are used herein are much larger than those reported in single-junction perovskite solar modules (table S4).

We fabricated 50 all-perovskite tandem solar modules with CDB and with a subcell width of 11.25 mm, which showed an average PCE of 20.9% (fig. S25A). The performance of single-junction WBG and NBG modules is summarized in fig. S27 and table S5. The champion tandem module exhibited a high PCE of 22.5% under reverse scan, with a *V*<sub>oc</sub> of 8.137 V, a *J*<sub>sc</sub> of 3.60 mA cm<sup>-2</sup>, and a FF of 76.8% (Fig. 3D). Considering a GFF of 93.3%, the active-area efficiency of the tandem module reached 24.1% (fig. S28). The tandem module showed a minor hysteresis between the reverse and forward scans (22.5 versus 22.1%) and a steady-state PCE of 22.5% at a MPP voltage of 6.7 V measured over 3 min (fig. S29).

**Fig. 4. Stability of all-perovskite tandem solar modules.**

**(A)** Continuous MPP tracking of an encapsulated tandem module over 500 hours under full simulated AM1.5 G illumination [100 mW cm<sup>-2</sup>, light-emitting diode (LED) simulator] in ambient air with a humidity of 30 to 50%. norm., normalized. **(B)** Thermal stability tracking of the tandem modules heated on an 85°C hotplate in a N<sub>2</sub> glove box. **(C)** The Ag 3d XPS spectra of the perovskite surfaces after peeling off the C<sub>60</sub>/ALD-SnO<sub>2</sub>/Ag stacks. The x-ray beam is located at the center of the exposed perovskite surface after peeling off the C<sub>60</sub>/ALD-SnO<sub>2</sub>/Ag stacks.



A single tandem module under illumination could steadily power a cooling fan (fig. S29 and movie S1), and six tandem modules connected in parallel could charge a smartphone (movie S2). One module was sent to an accredited independent PV calibration and measurement laboratory (Japan Electrical Safety and Environment Technology Laboratories) for certification. The module delivered a certified PCE of 21.7% (fig. S30), which has been included in recent solar cell efficiency tables (version 59) (5). The certified 21.7% PCE of the tandem module surpasses those of single-junction perovskite solar modules with areas >10 cm<sup>2</sup> (Fig. 3E and table S4). The PCE of our tandem cell (~1 cm<sup>2</sup>) using scalable fabrication delivered a performance comparable to that of tandem cells made by spin coating (table S6).

The encapsulated modules with CDB maintained their initial PCE after dark storage for 1778 hours under ambient conditions with a relative humidity of ~40% (fig. S31). We also tested the operating stability of encapsulated modules in ambient conditions under constant simulated 1-sun AM1.5 global (G) solar spectrum illumination. The module with CDB maintained 75% of its initial PCE (22.1%; fig. S32) after 500 hours of MPP tracking, whereas the module without CDB degraded to less than 50% of its initial PCE after 20 hours (Fig. 4A). We reasoned that the performance degradation of the module with CDB was not mainly attributed to the WBG perovskite; the single-

junction WBG module could maintain 95% of its initial PCE after 450 hours of MPP tracking (fig. S33). Two reasons for why the degradation of the tandem modules with CDB is faster than that of the single-junction WBG module could be (i) Au as a recombination layer could have diffused into the NBG perovskite layer, leading to the formation of defect states at the perovskite interface or in the bulk (18), and (ii) the reaction at the PEDOT:PSS/NBG perovskite interface may have led to poorer charge extraction (37).

We tracked the thermal stability of encapsulated modules by heating at 85°C in a N<sub>2</sub> glove box. The module without CDB degraded down to 10% of the initial PCE after 312 hours, whereas the module with CDB still maintained >70% of its initial performance (Fig. 4B). For modules without CDB, erosion of the metal electrode was observed after thermal aging at the interconnecting regions (fig. S34). We speculated that the erosion was induced by the halide-metal interdiffusion at the interconnecting regions (lateral edges of the subcells in the module) because of the direct contact between perovskite and metal. The halide-metal interdiffusion would have two negative effects: (i) Metal diffusion into the perovskite absorber could degrade the perovskite and increase charge carrier recombination, and (ii) the halide diffusion into the electrode could corrode the metal and reduce its electrical conduction.

To investigate the halide-metal diffusion, we reduced the subcell width in a tandem module to obtain 1-mm-wide grid cells at the P2 processing step to monitor the I-Ag interdiffusion through x-ray photoelectron spectroscopy (XPS) characterization (fig. S35). The devices were then subjected to heating at 85°C in a N<sub>2</sub> glovebox for 24 hours. For modules without CDB, Ag was detected by XPS in perovskite films when the x-ray beam was placed on the perovskite film surface after peeling off the multiple top layers of C<sub>60</sub>/ALD-SnO<sub>2</sub>/Ag (Fig. 4C and fig. S35). This result indicated that Ag diffused laterally from the P2 region into the perovskite absorbers, whereas the halides (I<sup>-</sup>) diffused into the edge metal electrode where they had direct contact with the perovskite (fig. S36). By contrast, for the CDB layer containing modules, no obvious signals of Ag (or I) were detected in the perovskite layer (or edge metal electrode), indicating that the I-Ag interdiffusion was effectively suppressed (18).

To intuitively elucidate the lateral interdiffusion between the perovskite and metal electrode, we further fabricated the following structures: (i) glass/ITO/~400-nm-thick WBG perovskite/Ag and (ii) glass/ITO/WBG perovskite/CDB/Ag, similar to the lateral structure in P2-scribed regions. After thermal aging at 85°C, we performed elemental analysis using SEM with energy-dispersive x-ray (fig. S37). The I-Ag interdiffusion occurred across the direct perovskite/electrode contact and extended over

the entire perovskite/metal layers, whereas the halide-metal interdiffusion was largely hindered by the use of CDB. Br-Ag interdiffusion was not observed (figs. S36 and S37), possibly because of the larger electronegativity of Br and thus stronger Pb-Br bonding (38).

We speculate that the CDB technique is a universal approach to enhance the efficiency and stability of all types of perovskite solar modules. To facilitate mass production in the future, development of a green solvent system (avoiding the use of toxic DMF) should be considered for the manufacturing of all-perovskite tandem solar modules (39, 40).

#### REFERENCES AND NOTES

- G. E. Eperon *et al.*, *Science* **354**, 861–865 (2016).
- K. Xiao *et al.*, *Nat. Energy* **5**, 870–880 (2020).
- R. Lin *et al.*, *Nat. Energy* **4**, 864–873 (2019).
- R. Lin *et al.*, *Nature* **603**, 73–78 (2022).
- M. A. Green *et al.*, *Prog. Photovolt. Res. Appl.* **30**, 3–12 (2022).
- J. E. Bishop, J. A. Smith, D. G. Lidzey, *ACS Appl. Mater. Interfaces* **12**, 48237–48245 (2020).
- X. Peng *et al.*, *Adv. Funct. Mater.* **27**, 1703704 (2017).
- Y. Deng *et al.*, *Nat. Energy* **3**, 560–566 (2018).
- M. Yang *et al.*, *Nat. Energy* **2**, 17038 (2017).
- Z. Yang *et al.*, *Sci. Adv.* **7**, eabg3749 (2021).
- J. B. Whitaker *et al.*, *Sustain. Energy Fuels* **2**, 2442–2449 (2018).
- J. Li *et al.*, *Joule* **4**, 1035–1053 (2020).
- N.-G. Park, *CrystEngComm* **18**, 5977–5985 (2016).
- Y. Rong *et al.*, *Science* **361**, eaat8235 (2018).
- Y. Hu *et al.*, *Joule* **3**, 2076–2085 (2019).
- E. Bi *et al.*, *Nat. Commun.* **8**, 15330 (2017).
- J. Li, Q. Dong, N. Li, L. Wang, *Adv. Energy Mater.* **7**, 1602922 (2017).
- H. Gao *et al.*, *Sol. RRL* **5**, 2100814 (2021).
- C. C. Boyd *et al.*, *ACS Energy Lett.* **3**, 1772–1778 (2018).
- Y. Deng *et al.*, *Nat. Energy* **6**, 633–641 (2021).
- Y. Deng *et al.*, *Sci. Adv.* **5**, eaax7537 (2019).
- S. Chen *et al.*, *Science* **373**, 902–907 (2021).
- H. Chen *et al.*, *Nature* **550**, 92–95 (2017).
- N. G. Park, K. Zhu, *Nat. Rev. Mater.* **5**, 333–350 (2020).
- Z. Liu *et al.*, *Nat. Energy* **5**, 596–604 (2020).
- E. Bi *et al.*, *Joule* **3**, 2748–2760 (2019).
- A. F. Palmstrom *et al.*, *Joule* **3**, 2193–2204 (2019).
- D. Zhao *et al.*, *Nat. Energy* **3**, 1093–1100 (2018).
- Z. Yang *et al.*, *Nat. Commun.* **10**, 4498 (2019).
- J. W. Yoo *et al.*, *Joule* **5**, 2420–2436 (2021).
- S. Jariwala *et al.*, *Joule* **3**, 3048–3060 (2019).
- Y. Zhao *et al.*, *Nat. Commun.* **11**, 6328 (2020).
- R. E. Beal *et al.*, *Matter* **2**, 207–219 (2020).
- K. A. Bush *et al.*, *ACS Energy Lett.* **3**, 428–435 (2018).
- L. A. Castriotta *et al.*, *Adv. Energy Mater.* **12**, 2103420 (2022).
- S. H. Reddy, F. Di Giacomo, A. Di Carlo, *Adv. Energy Mater.* **12**, 2103534 (2022).
- R. Prasanna *et al.*, *Nat. Energy* **4**, 939–947 (2019).
- J. Yang *et al.*, *Nano Energy* **54**, 218–226 (2018).
- L. Vesce *et al.*, *Sol. RRL* **5**, 2100073 (2021).
- R. Swartwout *et al.*, *Sol. RRL* **6**, 2100567 (2021).

#### ACKNOWLEDGMENTS

**Funding:** This work was financially supported by the National Natural Science Foundation of China (61974063, 61921005, and U21A2076), the Natural Science Foundation of Jiangsu Province (BK20202008 and BK20190315), Fundamental Research Funds for the Central Universities (0213/14380206 and 0205/14380252), the Frontiers Science Center for Critical Earth Material Cycling Fund (DLTD2109), the Program for Innovative Talents and Entrepreneurs in Jiangsu, and the Engineering and Physical Science Research Council, UK (EP/S004947/1). Y.H. acknowledges

support from the National University of Singapore (NUS) Presidential Young Professorship (R-279-000-617-133 and R-279-001-617-133). This work was authored in part by SERIS, a research institute at NUS. SERIS is supported by NUS, the National Research Foundation Singapore (NRF), the Energy Market Authority of Singapore (EMA), and the Singapore Economic Development Board (EDB). R.D.J.O. thanks the Penrose Scholarship for funding his studentship. **Author contributions:** H.T. conceived and directed the overall project. H.T. and H.J.S. supervised the research. K.X. fabricated all the devices and conducted the characterization. M.Z. fabricated NBG perovskite films, R.D.J.O. and Y.-H.L. carried out PLQY measurements, Z.L. carried out grazing-incidence wide-angle x-ray scattering characterizations, X.L. helped with module encapsulation and carried out transient photovoltage measurements, H.L. and R.L. carried out SEM characterizations, and J.X. helped with the ultraviolet-visible absorption and SEM with energy-dispersive x-ray characterizations. Y.H., X.W., and J.L. assisted with data analyses. K.X., Y.-H.L., D.L., Y.H., H.J.S., and H.T. wrote the manuscript. All authors read and commented on the manuscript. **Competing interests:** H.T. and K.X. are inventors on a patent application related to this work filed by Nanjing University. H.J.S. is a co-founder, Chief Scientific Officer, and director of Oxford PV Ltd., a company that is commercializing perovskite PVs. The other authors declare that they have no competing interests. **Data and materials availability:** All data are available in the main text or the supplementary materials.

#### SUPPLEMENTARY MATERIALS

science.org/doi/10.1126/science.abn7696  
Materials and Methods  
Figs. S1 to 38  
Tables S1 to S6  
References (41–47)  
Movies S1 and S2

Submitted 23 December 2021; accepted 5 April 2022  
10.1126/science.abn7696

## Scalable processing for realizing 21.7%-efficient all-perovskite tandem solar modules

Ke XiaoYen-Hung LinMei ZhangRobert D. J. OliverXi WangZhou LiuXin LuoJia LiDonny LaiHaowen LuoRenxing LinJun XuYi HouHenry J. SnaithHairen Tan

*Science*, 376 (6594), • DOI: 10.1126/science.abn7696

### Large-area tandem perovskite solar cells

Tandem solar cells allow more of the solar spectrum to be used. For all-perovskite implementations with large illumination areas, different band-gap compositions must be grown with fully scalable methods. Xiao *et al.* blade coated high-quality, wide-bandgap perovskite layers by tuning the cesium concentration in a mixed solvent system. They avoided diffusion between the perovskite layers with a tin oxide layer grown by atomic layer deposition that also served as an electron extractor. Small-area cells (1 square centimeter) have a power conversion efficiency (PCE) of about 25%, and a 20-square-centimeter module had a certified PCE of 21.7%. The encapsulated tandem module maintained more than 75% of its initial PCE after maximum power point operation for over 500 hours in ambient air. —PDS

### View the article online

<https://www.science.org/doi/10.1126/science.abn7696>

### Permissions

<https://www.science.org/help/reprints-and-permissions>

Use of this article is subject to the [Terms of service](#)

*Science* (ISSN ) is published by the American Association for the Advancement of Science, 1200 New York Avenue NW, Washington, DC 20005. The title *Science* is a registered trademark of AAAS.

Copyright © 2022 The Authors, some rights reserved; exclusive licensee American Association for the Advancement of Science. No claim to original U.S. Government Works